SIMULATION AND EXPERIMENTAL STUDY ON THE STABILITY OF AIRFLOW DISTRIBUTION ABOVE THE SCREEN IN AN AIR-SCREEN MILLET CLEANING DEVICE

1

谷子清选装置筛上气流分布稳定性仿真与试验研究

Dong-ming ZHANG, Zi-yang HUANG, Shu-juan YI*), Song WANG, Yi-fu CHEN

College of Engineering, Heilongjiang Bayi Agricultural University, Daqing/P. R. China *Tel:* +86-459-13836961877; *E-mail:* yishujuan_2005@126.com; Corresponding author: Shu-juan Yi

DOI: https://doi.org/10.35633/inmateh-77-26

Keywords: millet; air-sieve cleaning device; lattice Boltzmann method; airflow distribution stability

ABSTRACT

To investigate the influence of airflow distribution stability above the screen surface on the cleaning performance of an air-sieve millet cleaning device, this study employed the lattice Boltzmann method (LBM) to construct simulation models of screen surface flow fields with different screen types. The effects of airflow angle and airflow velocity on the distribution characteristics of airflow near and above the screen apertures were analyzed. The results showed that the flat square-hole screen exhibited high flow-field stability under various airflow conditions, whereas the perforated and fisheye screens were more susceptible to turbulent interference and had poorer uniformity. A simulation validation experiment was carried out using a self-developed airflow velocity and volume monitoring system, and the simulated and measured results showed high consistency in both variation trends and magnitudes, confirming the model's accuracy. Further bench-scale comparison tests indicated that the flat square-hole screen achieved the best cleaning performance, particularly when using the screen aperture combination of 10 mm (upper screen) and 8 mm (lower screen), resulting in the lowest loss rate and impurity rate. The findings of this study provide a theoretical basis and experimental reference for optimizing screen surface structures and improving the cleaning quality of millet cleaning devices.

摘要

为揭示风筛式谷子清选装置筛面气流分布稳定性对清选性能的影响规律,本研究采用格子玻尔兹曼方法(LBM)构建了不同筛型的筛面流场仿真模型,分析了气流角度与气流速度对筛孔附近及筛孔上方气流分布特性的作用机制。结果表明,平纹方孔筛在不同气流条件下均表现出较高的流场稳定性,而冲孔筛和鱼眼筛的流场分布易受湍流干扰且均匀性较差。基于自主设计的风速风量监测系统开展了仿真验证试验,仿真与实测结果在变化趋势及数量级上高度一致,验证了模型的准确性。进一步的台架对比试验表明,平纹方孔筛清选性能最优,尤其在上筛10 mm、下筛8 mm 的筛孔组合下,损失率最低且含杂率最小。本研究结果为优化谷子清选装置筛面结构、提升清选作业质量提供了理论依据和试验参考。

INTRODUCTION

As an important minor grain crop in China, millet serves as an effective supplement to staple cereals and occupies a significant position in the domestic coarse grain market (*Li et al.*, 2025). Among the post-harvest processing stages, cleaning is one of the critical steps that directly affects both yield and quality (*Wang et al.*, 2025; Fu et al., 2024). However, conventional cleaning equipment is poorly adapted to the small grain size and low bulk density of millet, making the cleaning process highly sensitive to variations in airflow during operation. The stability of airflow distribution across the screen surface has thus become a key factor influencing both grain loss and impurity rates during the cleaning of such small-seeded crops (*Li et al.*, 2022; Yang et al., 2025). This issue not only constrains improvements in the quality of millet harvesting, but also presents a major bottleneck to the advancement and broader adoption of mechanized harvesting technologies for millet.

In recent years, extensive research has been conducted by domestic scholars on cleaning technologies for various crops, with a primary focus on the optimization of equipment structure and key operational parameters (*Cleary et al., 2002; Dong et al., 2013; Yu et al., 2023*).

To enhance cleaning performance, researchers have proposed a range of innovative solutions tailored to the specific cleaning requirements of different crops (*Sun et al., 2024; Wang et al., 2021*). Structural innovations in cleaning devices have often incorporated principles of bionics and aerodynamic effects to optimize impurity removal and screening components, thereby improving adaptability, increasing efficiency, and reducing impurity content (*Bao et al., 2024; Wang et al., 2024; Wang et al., 2024*). In terms of parameter optimization, theoretical modeling and experimental validation have been employed to refine key variables such as feed rate, airflow velocity, and screen aperture size, contributing to improved cleaning effectiveness (*Zhang et al., 2025; Wang et al., 2021; Feng et al., 2023*). Moreover, many studies have utilized flow field analysis in combination with digital design and simulation techniques to optimize the cleaning process, with some results successfully applied to cleaning devices for crops such as maize, rapeseed, and millet (*Jiang et al., 2023; Ambrós et al., 2016*). Nevertheless, despite these advancements, a comprehensive understanding of airflow distribution patterns across the screen surface in air-sieve millet cleaning devices remains limited, indicating a pressing need for further in-depth investigation and mechanistic analysis.

In summary, although significant progress has been made in the structural optimization of cleaning devices, parameter tuning, and flow field analysis, systematic investigations into the stability of airflow distribution above the screen in air-sieve millet cleaning devices remain insufficient. In particular, there is a lack of quantitative analysis on the flow stability patterns of different screen types under various airflow conditions, and the correlation between simulation results and actual cleaning performance has not been adequately validated. To address these gaps, this study focuses on an air-sieve millet cleaning device and employs the lattice Boltzmann method to simulate the flow field over different screen types. A self-developed airflow velocity and volume monitoring system was employed for experimental validation, and bench-scale comparative tests were conducted to evaluate the cleaning performance of different screens. The objective was to elucidate the mechanism through which airflow distribution stability affects the quality of millet cleaning operations and to provide both theoretical and experimental support for screen optimization and performance improvement.

MATERIALS AND METHODS

Overall structure of the cleaning device

The experimental equipment employed was an air-sieve millet cleaning device, with its overall structure shown in Fig. 1. This device achieves effective separation of particles with different sizes or densities by precisely controlling the interaction between the airflow and the material, thereby enhancing cleaning efficiency and classification accuracy.

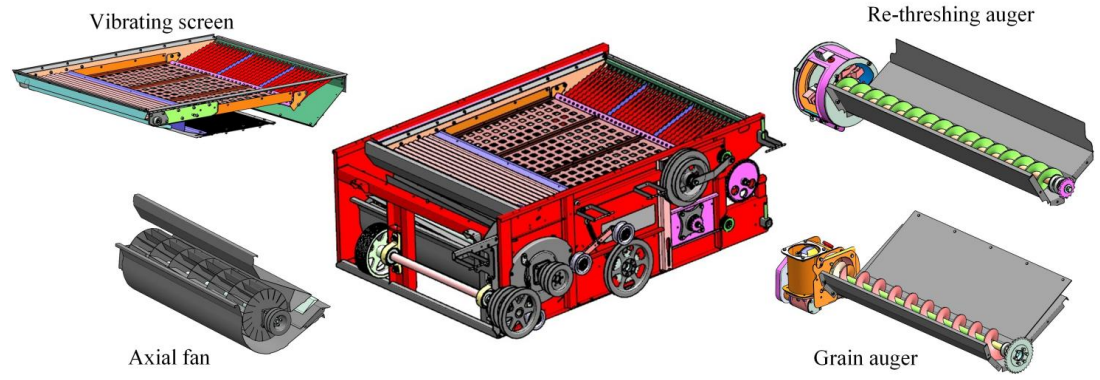


Fig. 1 - Air-sieve millet cleaning device

Lattice Boltzmann method

The lattice Boltzmann method (LBM) is a numerical approach developed based on discrete kinetic theory, and has been widely applied in the simulation of fluid dynamics, multiphase flows, heat transfer, and other complex physical systems. Its core concept originates from the Boltzmann equation, wherein the evolution of particle distribution functions is modeled over discrete time, space, and velocity lattices to describe the macroscopic behavior of fluid systems (*Eswaraiah et al., 2012; Zhang et al., 2024*).

The basic procedure for solving physical problems using the lattice Boltzmann method is illustrated in Fig. 2. In this study, LBM was employed to numerically analyze the internal flow field of the millet cleaning system, with a particular focus on how screen vibration and various types of discharged materials (e.g., millet grains and millet panicle clusters) influence the flow characteristics around the screen.

Compared with conventional macroscopic computational fluid dynamics (CFD) methods, the lattice Boltzmann method serves as a mesoscopic modeling approach that bridges the gap between microscopic and macroscopic scales. It offers superior adaptability and accuracy in simulating small-sized particles and geometrically complex materials typical of millet harvesting processes.

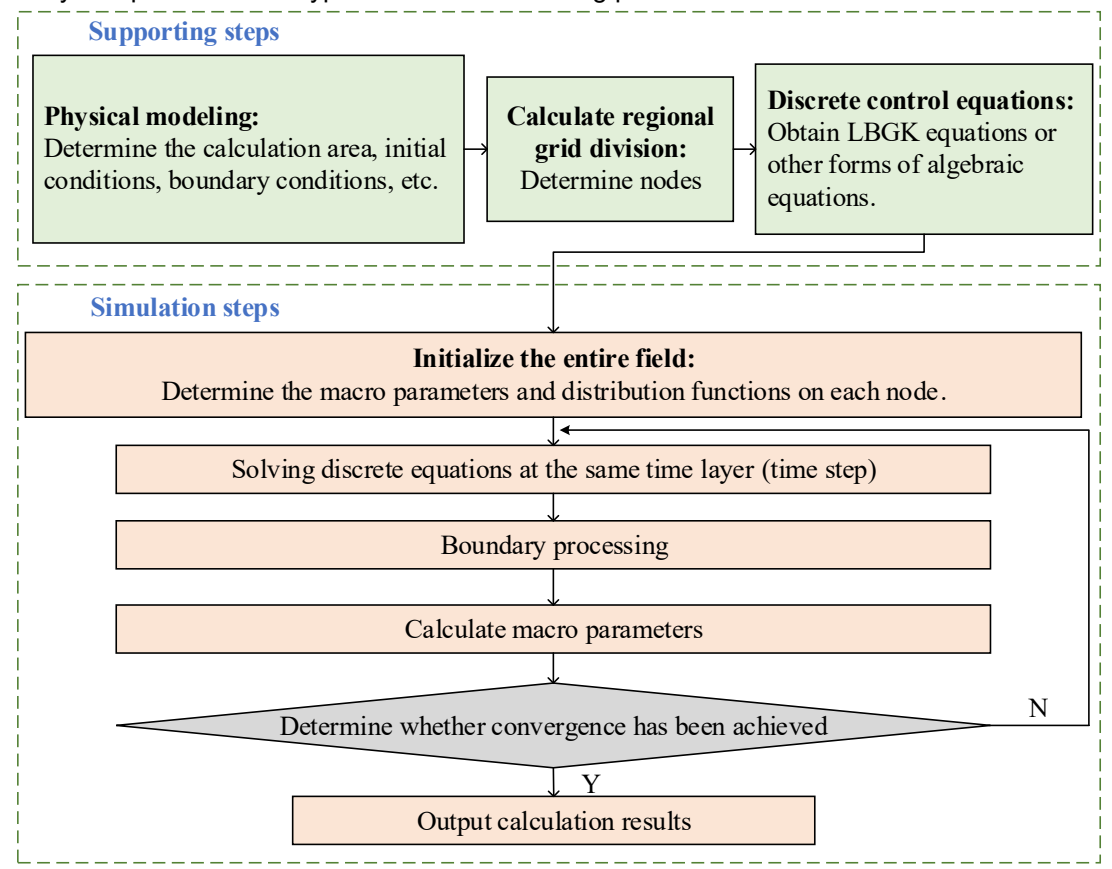
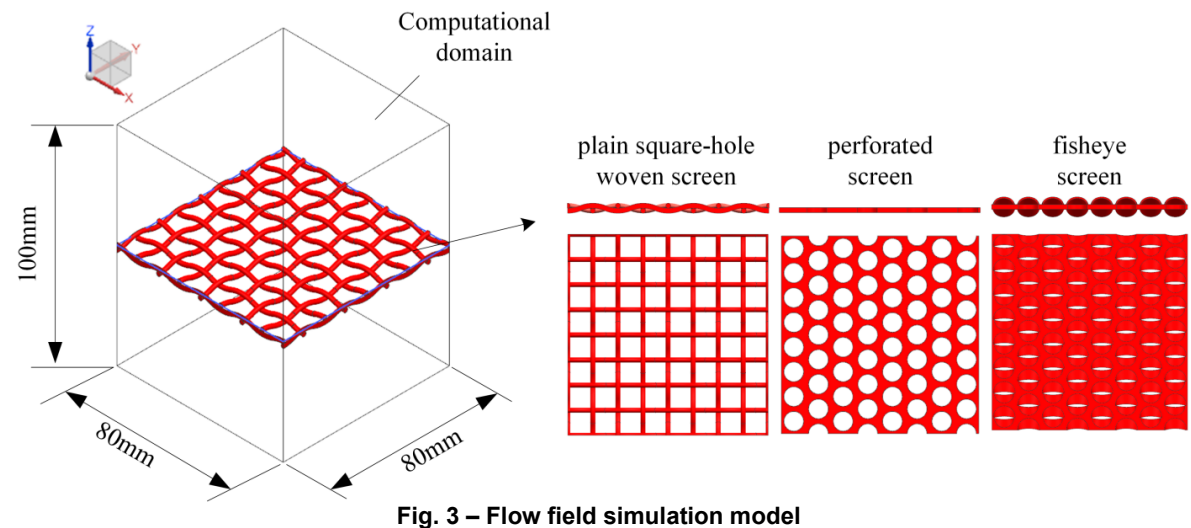


Fig. 2 - Lattice Boltzmann method solution process

Construction of the flow field simulation model

Three-dimensional geometric models of the flat square-hole screen, perforated screen, and fisheye screen were developed. Each model was trimmed to a standard size of 80 mm \times 80 mm using model editing functions. The computational domain was defined with dimensions of 80 mm \times 80 mm \times 100 mm, with the screen apertures oriented along the z-axis. The screen models were centrally positioned along the z-axis within the domain to ensure geometric symmetry. The final flow field simulation model is illustrated in Fig. 3.



Based on the established flow field simulation model, a series of simulation experiments were conducted to investigate the effects of airflow angle and velocity on the flow distribution across the screen surface. The simulation results were analyzed using post-processing tools, including flow visualization and virtual sensors.

Cross-sectional slices in the x–z plane near the screen apertures were extracted to observe the flow behavior and distribution. In each simulation case, two virtual velocity sensors were deployed: one positioned near the center of a screen aperture (Sensor 1) and the other located 30 mm above the aperture (Sensor 2). The sensor layout is illustrated in Fig. 4. The recorded velocity data, combined with flow field cross-sectional visualizations, enabled a comprehensive evaluation of flow distribution characteristics under various screen types and airflow conditions.

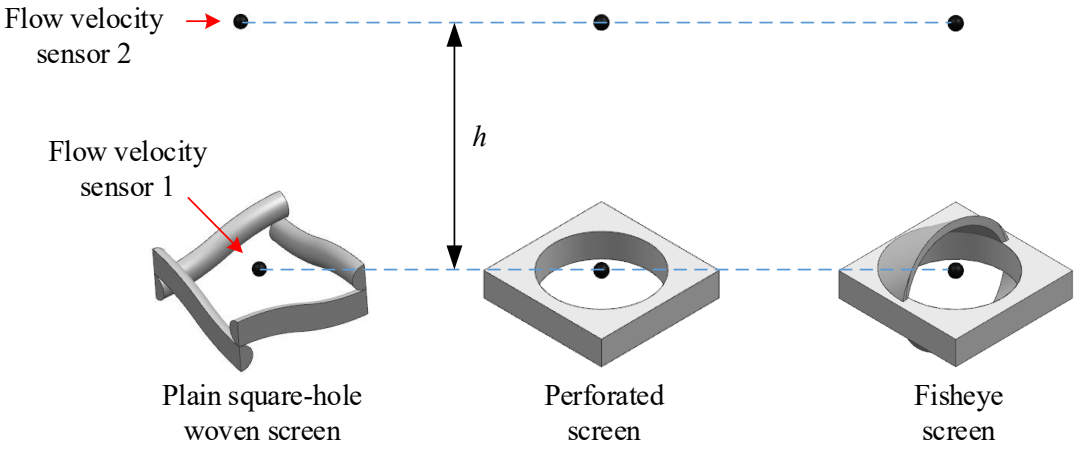


Fig. 4 - Virtual flow sensor location diagram

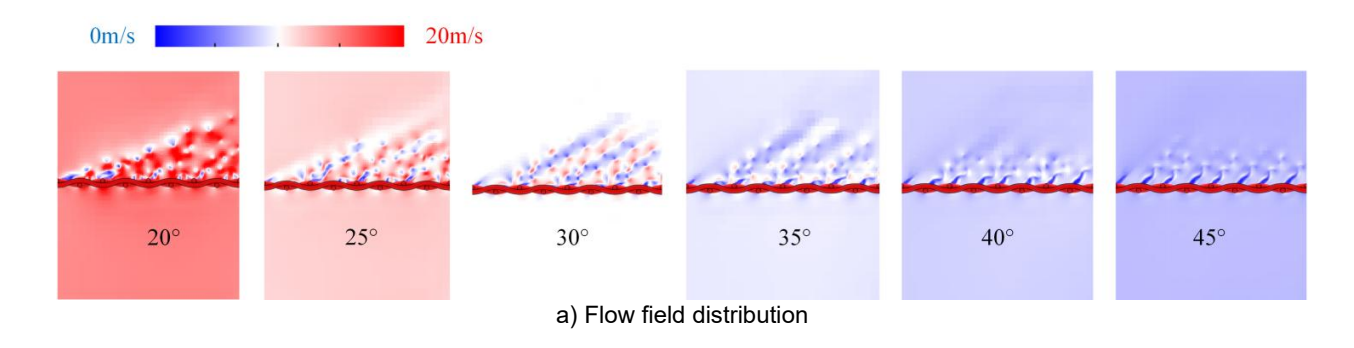
RESULTS AND DISCUSSIONS

Effect of airflow angle on flow field distribution

Simulation analysis of the flat square-hole screen under different airflow angles

To investigate the influence of airflow angle on the flow field distribution over the screen surface, simulation experiments were conducted for three screen types under varying airflow incidence angles. The flat square-hole screen was configured with aperture dimensions of 8 mm × 8 mm, while the perforated and fisheye screens were assigned circular apertures with an 8 mm diameter. During simulation, the velocity component in the z-direction was held constant at 5 m/s, while airflow angles were set at 20°, 25°, 30°, 35°, 40°, and 45°. The corresponding x-direction velocities were 13.74 m/s, 10.72 m/s, 8.66 m/s, 7.14 m/s, 5.96 m/s, and 5 m/s, respectively. These settings allowed for systematic analysis of how airflow incidence angle affects the flow behavior near and above the screen apertures.

The simulation results of the flat square-hole screen under different airflow angles are presented in Fig.5. Figure 5(a) illustrates the flow field distribution of the flat square-hole screen at the 50th simulation frame under various airflow angles. Figures 5(b) and 5(c) present the time-resolved velocity curves recorded by Sensor 1 (near the screen aperture) and Sensor 2 (30 mm above the aperture), respectively. The simulation results indicate that, with a constant airflow velocity in the z-direction, the peak airflow velocity near the screen apertures decreases with increasing airflow angle, corresponding to values of 19.75 m/s, 13.96 m/s, 11.00 m/s, 9.97 m/s, 10.53 m/s, and 7.71 m/s. Additionally, the fluctuation amplitude of the airflow near the apertures diminishes as the angle increases, with respective values of 12.55 m/s, 7.81 m/s, 7.61 m/s, 7.78 m/s, 4.62 m/s, and 0.96 m/s. In contrast, the airflow above the screen apertures remains relatively stable across all tested airflow angles.



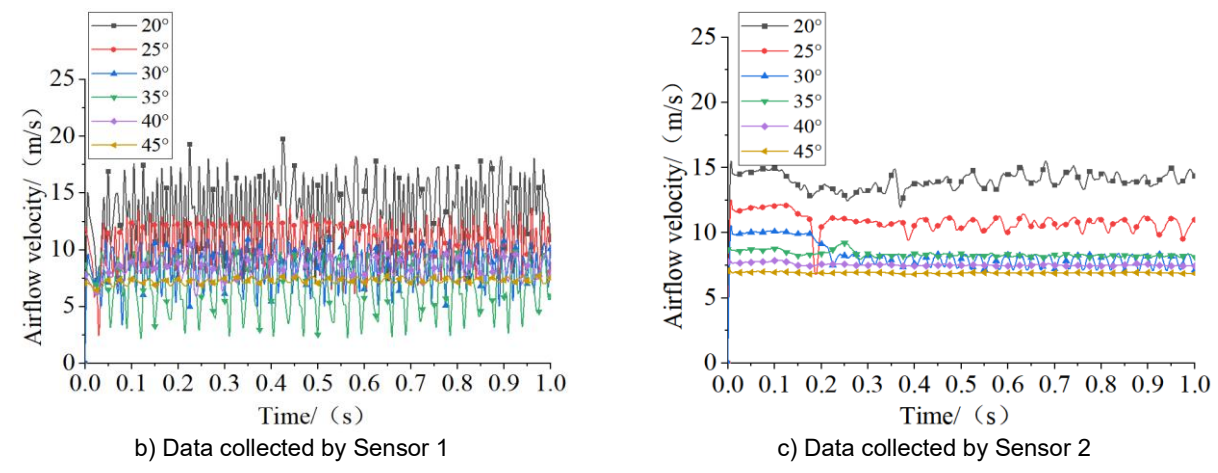


Fig. 5 - Flow field simulation of the flat square-hole screen at varying airflow angles

Simulation analysis of the perforated screen under different airflow angles

The flow field simulation results for the perforated screen under various airflow angles are presented in Fig. 6.

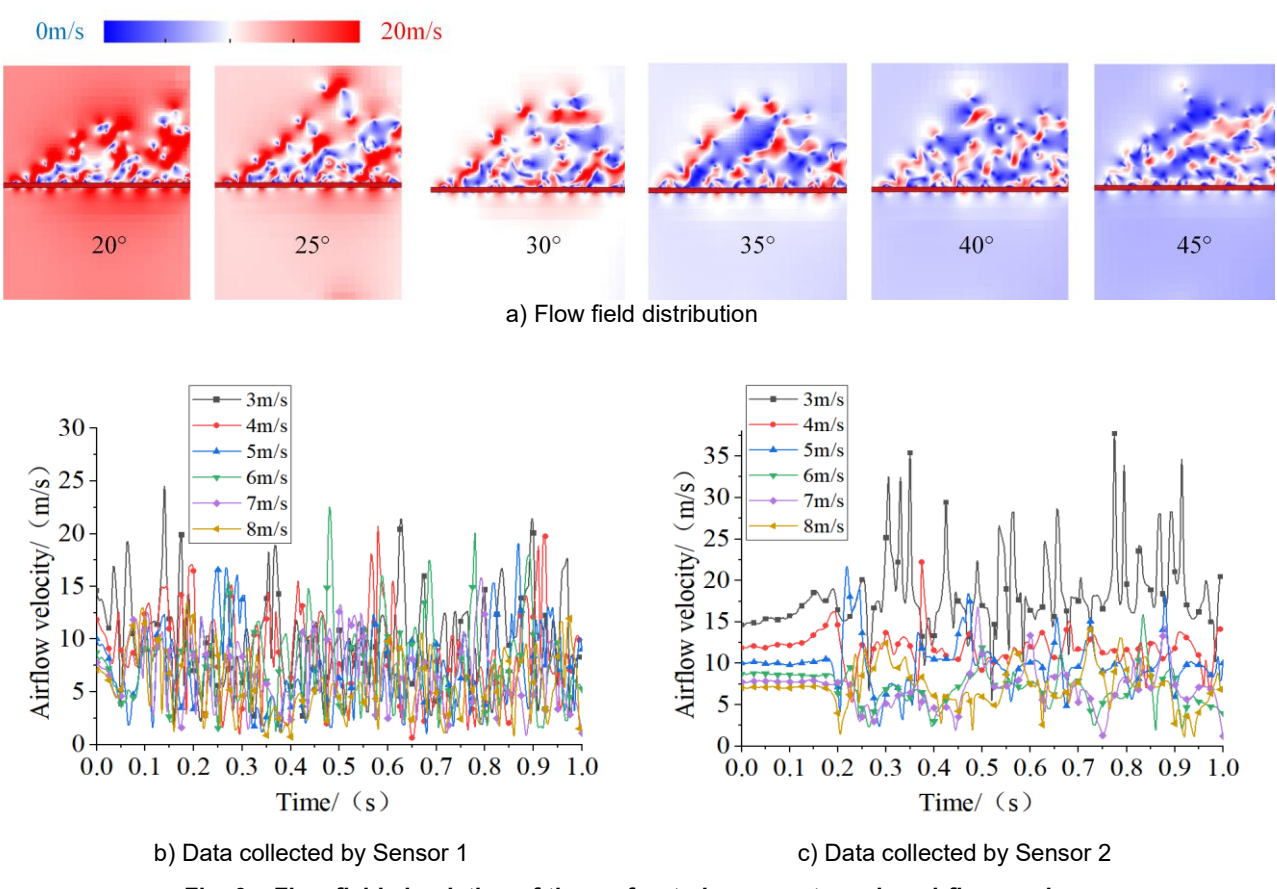


Fig. 6 – Flow field simulation of the perforated screen at varying airflow angles

Figure 6(a) shows the flow field distribution at the 50th frame of the simulation, while Figures 6(b) and 6(c) depict the time-varying velocity curves recorded by Sensor 1 and Sensor 2, respectively. The simulation results indicate that the flow stability near and above the screen apertures is relatively poor across all tested angles. The flow field visualization reveals the formation of noticeable turbulence as airflow passes through the perforated screen at different incident angles, resulting in uneven local distribution and reduced overall flow field uniformity.

Simulation analysis of the fisheye screen under different airflow angles

The simulation results for the fisheye screen under varying airflow angles are shown in Fig. 7.

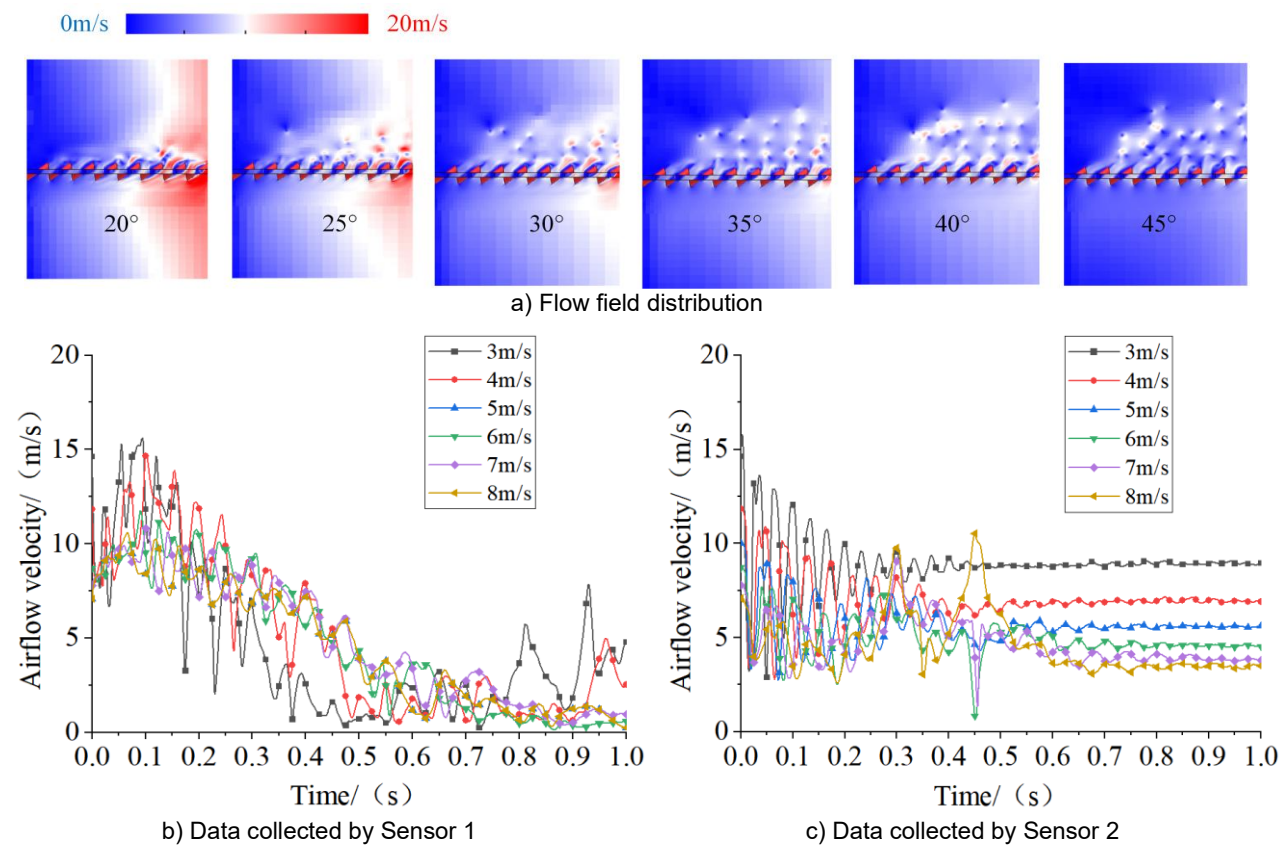


Fig. 7 - Flow field simulation of the fisheye screen at varying airflow angles

Figure 7(a) displays the flow field distribution at the 50th frame, while Figures 7(b) and 7(c) illustrate the time-dependent velocity curves recorded by Sensor 1 and Sensor 2, respectively. The results indicate that when the airflow angle is between 20° and 25°, the flow field near the screen apertures exhibits poor stability, with large velocity fluctuation amplitudes of 15.25 m/s and 13.83 m/s. As the airflow angle increases to 30° and beyond, the stability of the flow near the apertures improves, with the fluctuation amplitude decreasing to approximately 6–7 m/s. The velocity curves also reveal a general downward trend in airflow velocity as it passes through the aperture region. The flow field above the fisheye screen is also affected by turbulence. When the airflow angle ranges from 20° to 30°, the initial velocity fluctuations are relatively large but tend to stabilize over time. In contrast, for airflow angles between 35° and 45°, the initial fluctuations are smaller but increase gradually as time progresses.

In summary, the flat square-hole screen consistently demonstrates superior flow stability both near and above the screen apertures under different airflow angles. In contrast, both the perforated and fisheye screens are prone to turbulence. For the perforated screen, changes in airflow angle have minimal effect on improving flow uniformity. For the fisheye screen, increased airflow angles enhance flow stability near the apertures but simultaneously reduce stability in the region above the screen.

Effect of airflow velocity on flow field distribution

Simulation analysis of the flat square-hole screen under different airflow velocities

To investigate the effect of airflow velocity on the flow field distribution over the screen surface, simulation experiments were conducted for the three screen types under various airflow velocities. The flat square-hole screen was configured with aperture dimensions of 8 mm × 8 mm, while the perforated and fisheye screens were assigned circular apertures with a diameter of 8 mm. The airflow angle relative to the horizontal plane was fixed at 30°, and the z-direction airflow velocity was set to 3 m/s, 4 m/s, 5 m/s, 6 m/s, 7 m/s, and 8 m/s. The corresponding x-direction velocities were 5.20 m/s, 6.93 m/s, 8.66 m/s, 10.39 m/s, 12.12 m/s, and 13.86 m/s. These settings enabled a systematic analysis of how varying airflow velocity affects the structure and stability of the flow field across different screen types.

Time/(s)

c) Data collected by Sensor 2

20m/s 3m/s4m/s5m/s7m/s8m/s 6m/s Flow field distribution a) 3m/s 3m/s4m/s4m/s 25 5m/s5m/s 25 6m/s6m/s7m/sAirflow velocity/ (m/s) 7 m/s20 8m/s8m/s0.3 0.4 0.5 0.6 0.7 0.8 0.1 0.2 0.0 0.1 0.2 0.3 0.4 0.5 0.6 0.7 0.8 0.9 1.0

The simulation results for the flat square-hole screen under different airflow velocities are shown in Fig.8.

Fig. 8 - Flow field simulation of the flat square-hole screen at varying airflow velocities

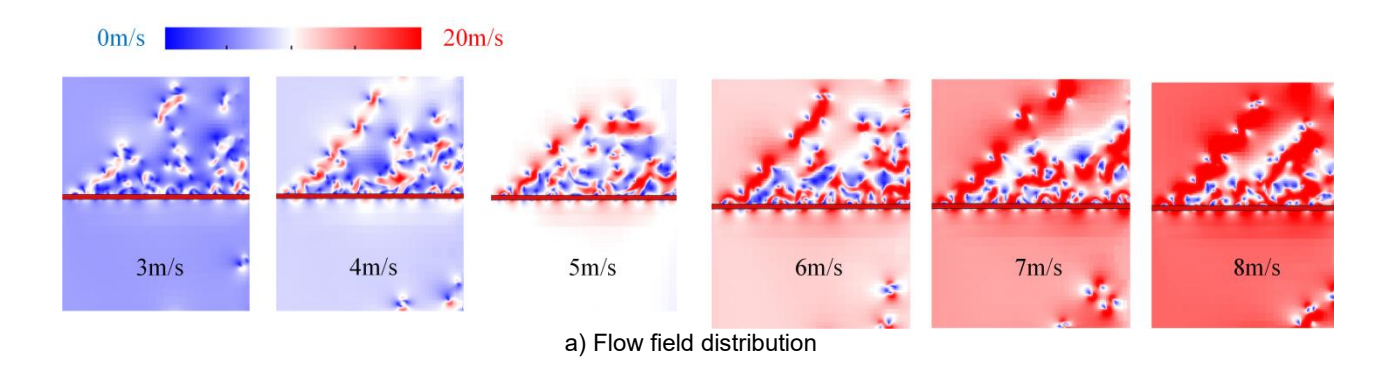
Figure 8(a) illustrates the flow field distribution of the flat square-hole screen at the 50th simulation frame under different airflow velocities. Figures 8(b) and 8(c) present the time-dependent velocity curves recorded by Sensor 1 and Sensor 2, respectively. The simulation results indicate that the airflow near the screen apertures exhibits clear periodic fluctuations, with the amplitude increasing significantly as the airflow velocity increases. For z-direction velocities ranging from 3 m/s to 8 m/s, the corresponding fluctuation amplitudes were 4.39 m/s, 5.95 m/s, 7.61 m/s, 8.65 m/s, 8.39 m/s, and 11.83 m/s, respectively. In contrast, the airflow above the apertures remained relatively stable, with velocity increasing as the initial airflow velocity increased, but without notable influence on flow field stability.

Simulation analysis of the perforated screen under different airflow velocities

Time/(s)

b) Data collected by Sensor 1

The simulation results of the flow field for the perforated screen under different airflow velocities are shown in Fig. 9.



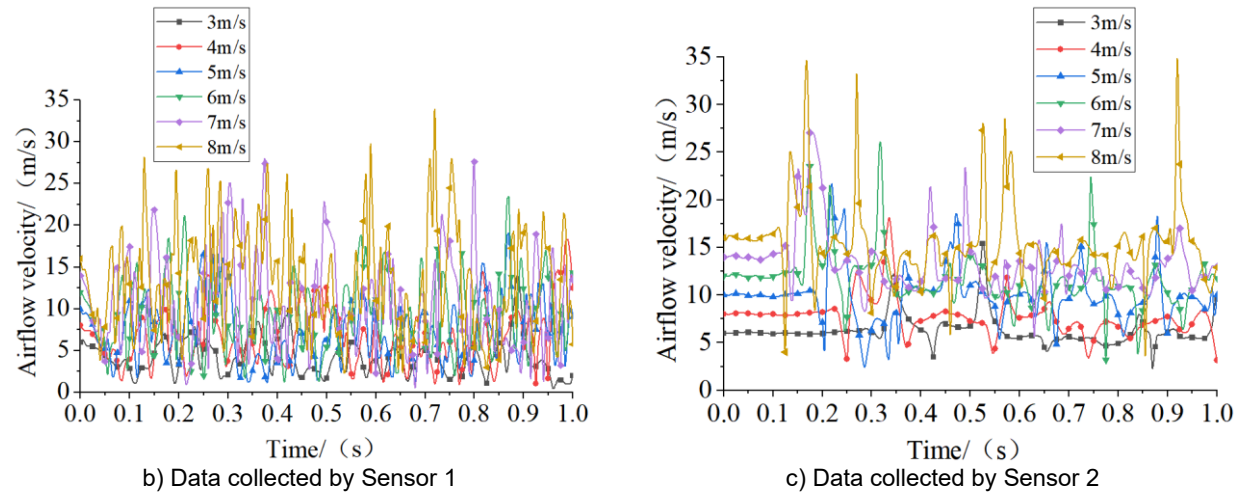


Fig. 9 - Flow field simulation of the perforated screen at varying airflow velocities

Figure 9(a) shows the flow field distribution of the perforated screen at the 50th frame under various airflow velocities, while Figures 9(b) and 9(c) present the time-varying velocity curves captured by Sensor 1 and Sensor 2, respectively. The simulation results indicate that as the airflow velocity increases, the flow field stability both near and above the screen apertures deteriorates significantly. The fluctuation amplitudes of airflow velocity near the apertures were 8.75 m/s, 12.72 m/s, 15.44 m/s, 19.34 m/s, 26.55 m/s, and 24.38 m/s, respectively. For the region above the apertures, the corresponding amplitudes were 14.72 m/s, 19.16 m/s, 18.76 m/s, 18.77 m/s, and 29.65 m/s. As revealed by the flow field visualizations, higher initial airflow velocities lead to stronger turbulence after passing through the screen, thereby reducing the uniformity and stability of the local flow distribution.

Simulation analysis of the fisheye screen under different airflow velocities

The simulation results of the flow field for the fisheye screen under different airflow velocities are shown in Fig.10.

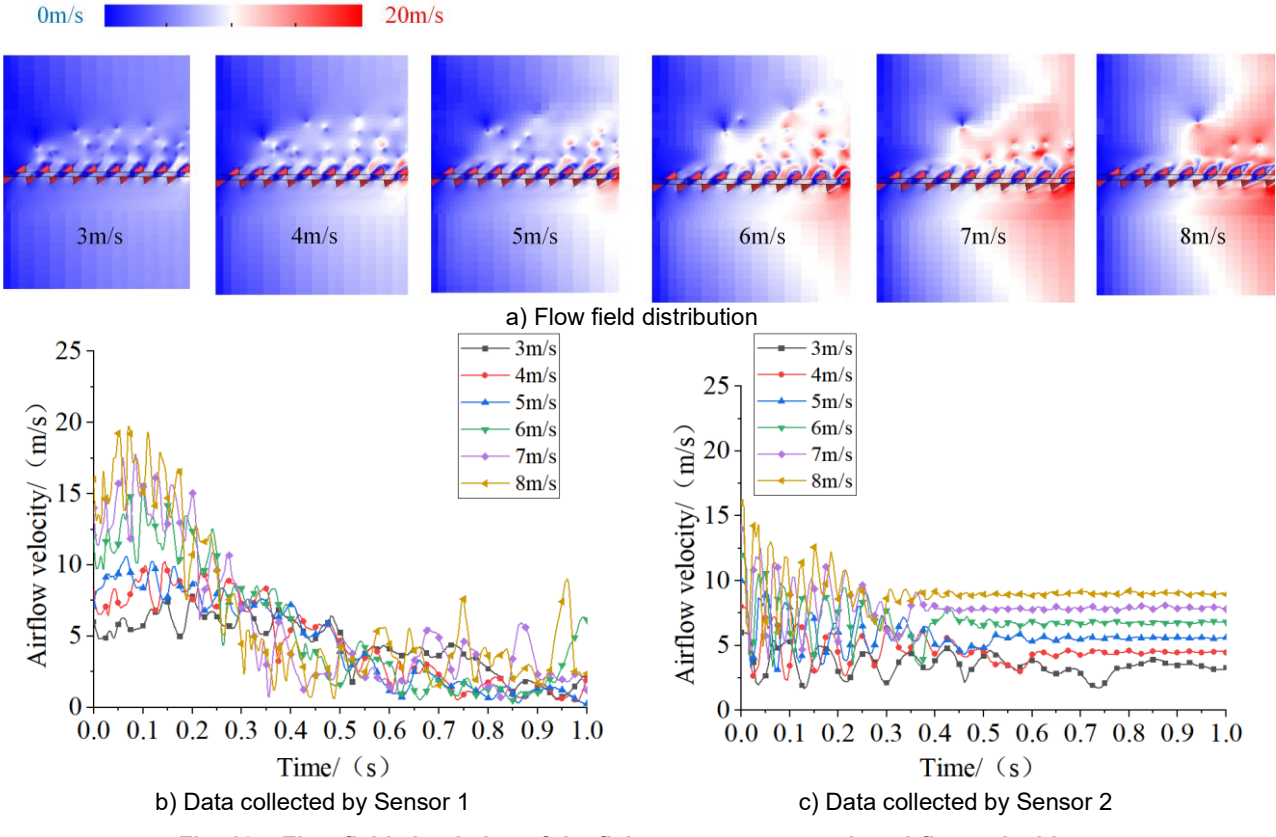


Fig. 10 - Flow field simulation of the fisheye screen at varying airflow velocities

Figure 10(a) shows the flow field distribution of the fisheye screen at the 50th simulation frame under various airflow velocities, while Figures 10(b) and 10(c) present the time-resolved velocity curves obtained from Sensor 1 and Sensor 2, respectively. The simulation results indicate that the flow distribution behavior of the fisheye screen under varying airflow velocities is similar to that of the perforated screen. As the airflow velocity increases, the stability of the flow field near and above the screen apertures declines, accompanied by more pronounced fluctuations and enhanced turbulence characteristics.

In summary, airflow velocity has a pronounced influence on the stability of flow field distribution across different screen types, with the underlying mechanisms varying according to screen geometry. For the flat square-hole screen, increasing airflow velocity results in only moderate periodic fluctuations near the apertures, while the flow field above the screen remains relatively stable. This indicates a strong resistance to turbulence and good overall flow uniformity, highlighting the structural advantages of this screen type. In contrast, the perforated and fisheye screens exhibit substantial instability at higher airflow velocities. The airflow passing through these screens tends to generate intense turbulence, causing significant velocity fluctuations both near and above the apertures, with the effect being most severe in the perforated screen. These findings further emphasize the critical role of screen geometry in determining airflow control characteristics during the cleaning process, and provide valuable theoretical support for screen structure optimization and airflow parameter configuration in air-sieve systems.

Validation test of the flow field simulation

Composition of the airflow velocity and volume monitoring system

To verify the reliability of the flow-field simulation data, an airflow velocity and volume monitoring system was designed and implemented for the air-sieve millet cleaning device, as illustrated in Fig. 11. The system consists of a PLC control unit, computer-based monitoring software, airflow velocity and volume sensors, and data acquisition probes. The probes can be installed at ten fixed sampling points above the screen surface or repositioned freely to any desired location, enabling dynamic monitoring and real-time recording of airflow velocity and volume at various positions.

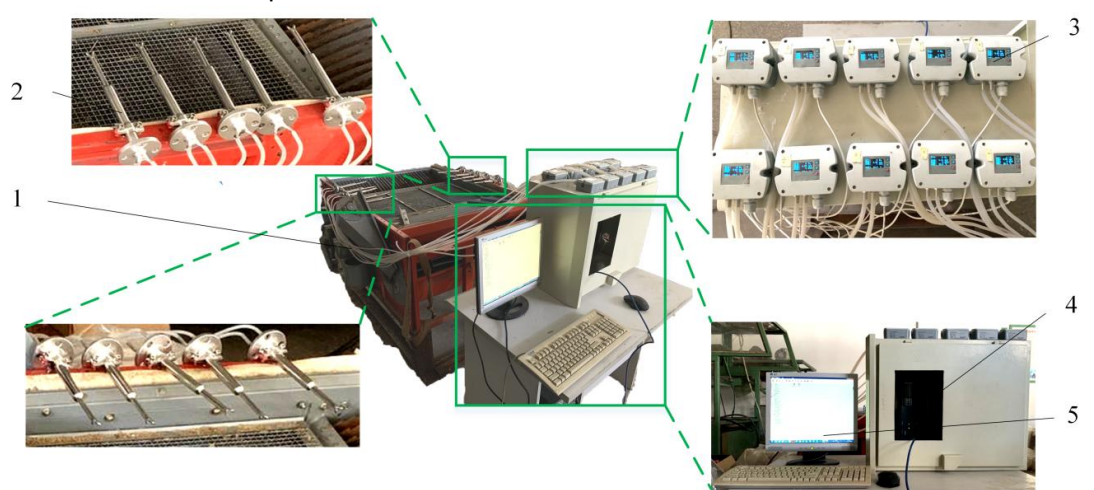


Fig. 11 – Airflow velocity and volume monitoring system

1. Air-sieve millet cleaning device; 2. Airflow velocity and volume probe; 3. Airflow velocity and volume sensor;

4. PLC control unit; 5. Computer-based monitoring software system

The hardware of the PLC-controlled airflow velocity and volume acquisition system consists of a Siemens S7-200 Smart variable-frequency controller, a 972-0BB12-0XA0 DP bus connector, a Siemens PM207 power supply (24 V DC/5A), as well as circuit breakers and control buttons. The S7-200 Smart controller offers high scanning speed and processing efficiency, with a basic instruction execution time of up to 0.15 µs. It is equipped with built-in Modbus RTU and USS protocol libraries, enabling superior performance in Modbus master/slave data communication, equal-byte data exchange, and CRC table initialization—approximately 20 times faster than other controllers in the same class.

The PM207 power supply simultaneously provides power to both the controller and ten connected JY-GD680 airflow velocity and volume sensors (rated for 24 V AC/DC ± 20%). These sensors measure airflow velocity in the range of 0–50 m/s with a resolution of 0.01 m/s. The corresponding airflow probe is an S-type Pitot tube (Model YQS-250), which captures real-time airflow velocity and volume data within the flow field of the cleaning device. The measured data are displayed on the sensor LCD screens and transmitted to a computer via Ethernet for real-time recording and storage.

The system software was developed on the MCGS (Monitor and Control Generated System) platform and supports real-time monitoring of multiple parameters, including airflow velocity, airflow volume, air pressure, and temperature. The complete hardware architecture of the airflow velocity and volume acquisition system is shown in Fig. 12.

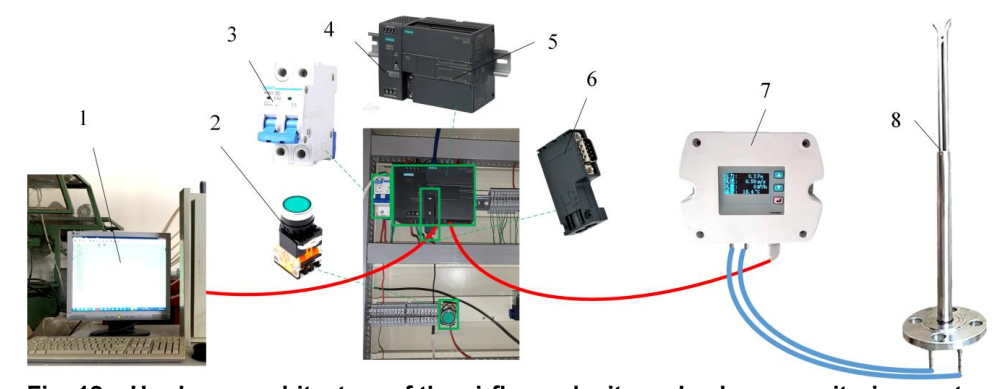


Fig. 12 – Hardware architecture of the airflow velocity and volume monitoring system

1. Computer; 2. Control button; 3. Air switch; 4. PLC power supply; 5. S7-200 Smart PLC; 6. DP bus connector;

7. Airflow velocity and volume sensor; 8. Airflow velocity and volume probe

Validation test

To evaluate the operational performance of the airflow velocity and volume monitoring and acquisition system, a validation experiment was carried out on the air-sieve millet cleaning device. The operating parameters of the cleaning device were configured according to the conditions defined in the simulated model of airflow through a dynamic screen, ensuring consistency between the experimental and simulation setups. Specifically, the vibrating screen was operated at an amplitude of 20 mm and a frequency of 7 Hz. To maintain positional consistency, the physical measurement points were aligned with the virtual sensor locations used in the simulation, as illustrated in Fig. 13.

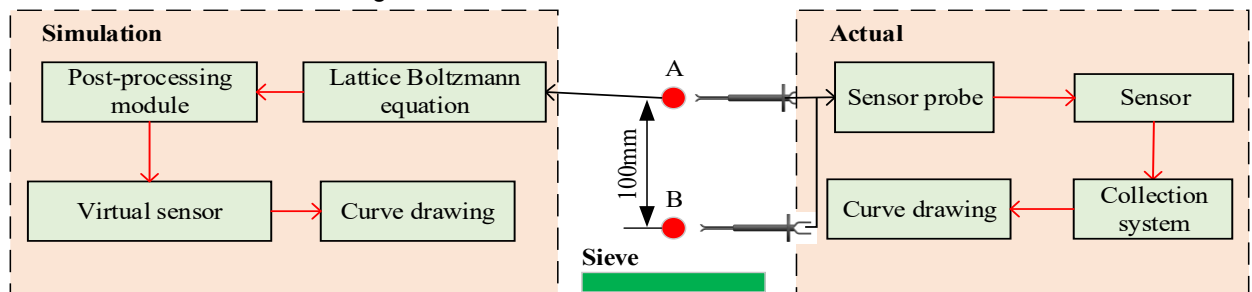
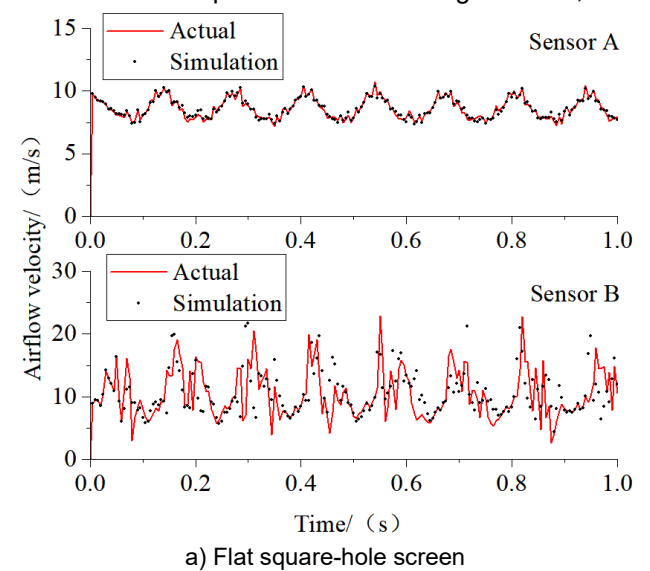


Fig. 13 - Sensor layout and data acquisition workflow for simulation and experimental validation

Two representative points near the screen apertures, denoted as points A and B, were selected for airflow velocity data acquisition. Corresponding virtual sensors A and B were placed in the simulation model, and their simulated velocity data were exported. For each of the three screen types, comparative plots of the measured and simulated airflow velocities at points A and B were generated, as shown in Fig. 14.



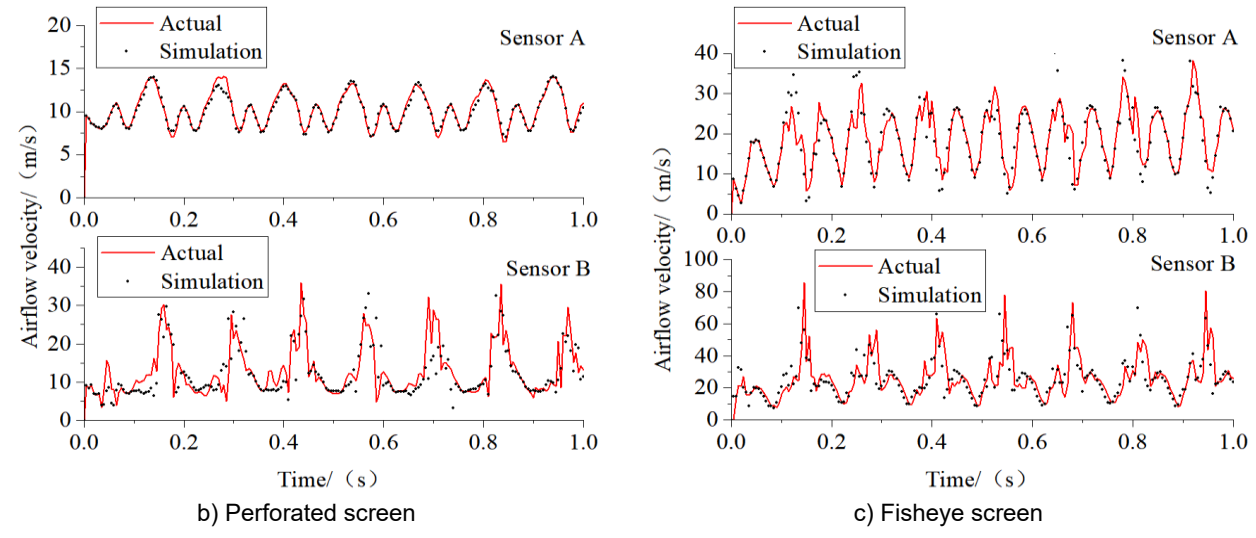


Fig. 14 - Comparison between simulation and experimental data

In Fig. 14, the red curve represents the airflow velocity data acquired by the monitoring system, while the black scatter points denote the corresponding simulation results. Statistical analysis indicates that the airflow velocity exhibits a periodic variation pattern, with notable differences between points A and B: point A shows relatively small fluctuations, whereas point B experiences significantly larger ones.

At point B, for all three screen types, the simulation results agree well with the experimental data, with most simulated points falling close to the measured curve and following similar trends. Although the overall pattern remains periodic, the fluctuations within each individual peak are irregular and display considerable variability. Specifically, the airflow velocity fluctuation ranges at point B are as follows: 2.08-27.77 m/s for the flat square-hole screen, 3.41-40.46 m/s for the perforated screen, and 7.86-85.53 m/s for the fisheye screen.

At point A, the agreement between the simulated and measured results remains strong. The airflow velocity curve for the flat square-hole screen closely resembles a sinusoidal waveform, with a range of 7.19-10.73 m/s. For the perforated screen, the airflow velocity profile within a single vibration cycle exhibits a dual-peak structure, with the major and minor peaks reaching 14.41 m/s and 11.89 m/s, respectively. A similar dual-peak pattern is observed for the fisheye screen, with an overall velocity range of 2.56-38.27 m/s and a secondary peak value of 27.15 m/s.

These results demonstrate a strong correlation between the simulated and experimental data in both trend and magnitude, confirming the accuracy of the simulation model. Furthermore, the observed airflow fluctuation characteristics indicate that the flat square-hole screen provides superior flow-field stability near the screen apertures compared with the other two screen types, which is consistent with the results obtained from the simulated flow-field cross-sections.

The validation test results demonstrate that the airflow velocity data acquired by the monitoring system are highly consistent with the simulation results in terms of curve shape, variation trend, and magnitude. This confirms the reliability of both the data acquisition method and the structural design of the monitoring system. Furthermore, the results verify the applicability of the lattice Boltzmann method for simulating the flow field during millet cleaning with discharged materials, as well as the accuracy and feasibility of the static and dynamic screen surface flow-field simulation models.

Bench-scale validation test

Test factors and evaluation indices

The objective of the bench-scale experiment is to validate the accuracy of the simulation analysis through physical testing. Based on previous simulation results, the flat square-hole screen exhibits a more stable flow field distribution under identical airflow conditions, which is conducive to improving the quality of the cleaning operation. To compare the operational performance of the three screen types in millet cleaning, a controlled variable method was employed to investigate the cleaning performance of the device under different screen aperture configurations.

Two evaluation indices were selected for the test: grain loss rate and impurity rate, which were calculated according to Equations (1) and (2), respectively.

$$y_{s} = 1 - \frac{m_{1}}{m_{2}} \tag{1}$$

$$y_{s} = 1 - \frac{m_{1}}{m_{2}}$$

$$y_{z} = 1 - \frac{m_{1}}{m_{3}}$$
(1)

where y_s is the grain loss rate, %; y_z is the impurity rate, %; m_l is the mass of grain collected below the screen, g; m_2 is the total mass of grain fed into the device, g; m_3 is total mass of material passing through the screen, g.

Experimental results

Based on the preceding simulation analysis, a bench-scale comparative experiment was conducted. A controlled variable method was employed, with the test parameters uniformly set as follows: vibration amplitude of 20 mm, vibration frequency of 7 Hz, airflow velocity of 5 m/s, and an airflow angle of 30° relative to the horizontal plane. Since screen aperture size has a significant effect on the screening performance of different screen types, and considerable performance differences may still occur even under identical aperture sizes, efforts were made to eliminate this variable's influence. Referring to the results of the particle screening simulation, the upper screen apertures for the three screen types were set to 10 mm, 12 mm, and 14 mm, respectively, with corresponding lower screen aperture sizes of 8 mm, 10 mm, and 12 mm. The experimental results are summarized in Table 1.

> Table 1 Comparative test results

Comparative test results							
No.	Screen aperture size	Flat square-hole screen		Perforated screen		Fisheye screen	
		y s/ (%)	y₂/ (%)	y s/ (%)	yz/ (%)	y s/ (%)	y₂/ (%)
1	upper screen 10mm lower screen 8mm	4.06	5.34	7.85	8.08	12.88	7.56
2	upper screen 12mm lower screen 10mm	4.11	5.87	6.49	8.53	10.50	7.94
3	upper screen 14mm lower screen 12mm	4.09	6.95	6.52	10.14	10.34	8.16

According to the experimental results, when using the flat square-hole screen, the grain loss rate remained largely constant as screen aperture size increased, while the impurity rate showed a slight upward trend. The best cleaning performance was achieved with an upper screen size of 10 mm and a lower screen size of 8 mm. For the perforated screen, an increase in aperture size led to a noticeable reduction in loss rate, but was accompanied by an increase in impurity rate; the optimal performance was observed with the 12 mm upper and 10 mm lower screen configuration. In the case of the fisheye screen, larger apertures also resulted in reduced loss rates, while the impurity rate remained relatively unchanged. Better performance was achieved under the 12 mm/10 mm and 14 mm/12 mm configurations.

Overall, the flat square-hole screen consistently outperformed the other two screen types under all aperture configurations, with the 10 mm upper and 8 mm lower screen combination delivering the best cleaning results.

These findings validate the simulation results and confirm the reliability of using the lattice Boltzmann method for flow field stability analysis. They also highlight the direct influence of screen flow field stability on the cleaning quality of millet harvesting operations.

CONCLUSIONS

(1) A flow-field simulation model of the screen surface in an air-sieve millet cleaning device was established based on the Lattice Boltzmann Method (LBM). The effects of screen type, airflow angle, and airflow velocity on the stability of airflow distribution above the screen were systematically analyzed. The simulation results showed that the flat square-hole screen maintained stable airflow near and above the apertures under various conditions, whereas the perforated and fisheye screens were more susceptible to turbulence and exhibited lower flow uniformity.

- (2) An airflow velocity and volume monitoring system was developed and employed for validation experiments. The simulation results showed strong agreement with the measured data in both trend and magnitude, confirming the accuracy and applicability of the LBM-based simulation model for predicting airflow distribution in millet cleaning devices.
- (3) Bench-scale comparative experiments further demonstrated that screen type significantly influences cleaning performance. The flat square-hole screen consistently outperformed the other two screen types, particularly under the 10 mm upper screen and 8 mm lower screen configuration, which yielded the lowest grain loss and impurity rates. These findings validate the direct influence of screen surface flow stability on cleaning quality and provide both theoretical and experimental support for optimizing screen design in air-sieve millet cleaning systems.

ACKNOWLEDGEMENT

This research was supported by the Heilongjiang Provincial Postdoctoral Science Foundation (LBH-Z24251), the Guiding Science and Technology Project of Daqing City (zd-2025-033), the Research Start-up Program for Returned and Introduced Talents (XYB202309), and the "Sanzong" Youth Innovation Talent Program (ZRCQC202304).

REFERENCES

- [1] Ambrós, W., Cazacliu, B., & Sampaio, C. (2016). Wall effects on particle separation in air jigs. *Powder Technology*, Vol. 301, pp. 369-378.
- [2] Bao, G., Zhang, Z., Yang, X., Liu, L., Li, J., Lv, Z., & Yang, W. (2024). Design and experiment of separating impurities device for corn plot test harvester based on Coanda effect. *Transactions of the Chinese Society for Agricultural Machinery*, Vol. 55, Issue 10, pp. 234-243.
- [3] Cleary, P. W., & Sawley, M. L. (2002). DEM modelling of industrial granular flows: 3D case studies and the effect of particle shape on hopper discharge. *Applied Mathematical Modelling*, Vol. 26(2), 89-111.
- [4] Dong, K., Wang, B., & Yu, A. (2013). Modeling of particle flow and sieving behavior on a vibrating screen: From discrete particle simulation to process performance prediction. *Industrial & Engineering Chemistry Research*, Vol. 52, Issue 33, pp. 11333-11343.
- [5] Eswaraiah, C., Angadi, S. I., & Mishra, B. K. (2012). Mechanism of particle separation and analysis of fish-hook phenomenon in a circulating air classifier. *Powder Technology*, Vol. 218, pp. 57-63.
- [6] Feng, X., Wang, L., Yu, K., Gao, Y., Bi, S., & Wang, B. (2023). Design and experiment of mechanism of wave screen for maize grain cleaning. *Transactions of the Chinese Society for Agricultural Machinery*, Vol. 54, Issue 4, pp. 142-154.
- [7] Fu, J., Zhang, J., & Liu, F. (2024). Enhanced sieving mechanism of novel cleaning screen and investigation of particle movement characteristics on the screen. *Powder Technology*, Vol. 431, pp. 119043-119047.
- [8] Jiang, T., Li, H., Guan, Z., Mu, S., Wu, C., & Zhang, M. (2023). Design and experiments of material uniform dispersion and diversion device on cleaning screen surface for oilseed harvesting. *Transactions of the Chinese Society for Agricultural Machinery*, Vol. 54, Issue 1, pp. 146-158.
- [9] Li, A., Wen, W., & Wang, K. (2025). Research on the development status and countermeasures of the modern agricultural standardization system for millet. *Standard Science*, Vol. 2025, Issue 7, pp. 109-115.
- [10] Li, Y., Xu, L., Lv, L., Shi, Y., & Yu, X. (2022). Study on modeling method of a multi-parameter control system for threshing and cleaning devices in the grain combine harvester. *Agriculture*, Vol. 12(9), 1483.
- [11] Sun, T., Wu, B., Zhang, H., Han, Y., Liu, H., & Zhang, Y. (2024). Discrete element simulation of particle flow and separation in a vibrating screen with variable rectangular hole screen. *Powder Technology*, Vol. 434, pp. 119305-119317.
- [12] Wang, B., Yu, Z., Hu, Z., Cao, M., Zhang, P., & Wang, B. (2021). Numerical simulation and experiment of flow field in three air systems of air separation system of peanut pickup harvester. *Transactions of the Chinese Society for Agricultural Machinery*, Vol. 52, Issue 11, pp. 103-114.
- [13] Wang, C., Jin, C., Yang, X., Lei, C., Li, P., & Zhao, Z. (2025). Research status and development trend of screening devices for grain combine harvesters. *Journal of Chinese Agricultural Mechanization*, Vol. 46, Issue 6, pp. 46-54.
- [14] Wang, C., Liu, Q., & Yang, L. (2024). The MFBD-DEM coupling simulation approach for the investigation of granules screening efficiency in 4-DOF flip-flow screen. *Granular Matter*, Vol. 26, Issue 1, pp. 1.

- [15] Wang, F., Li, B., Zhu, R., Wang, S., Liu, Y., Gao, X., & Yang, X. (2024). Design and test of the wind-sieve type cleaning equipment for cumin threshing machine. *Transactions of the Chinese Society of Agricultural Engineering (Transactions of the CSAE*), Vol. 40, Issue 22, pp. 39-50.
- [16] Wang, L., Song, L., Feng, X., Wang, H., & Li, Y. (2021). Research status and development analysis of screening devices of grain combine harvester. *Transactions of the Chinese Society for Agricultural Machinery*, Vol. 52, Issue 6, pp. 1-17.
- [17] Yang, R., Wang, S., Pan, Z., Li, G., Shu, Y., Liu, Q., Liu, Z., & Miao, Y. (2025). Design and experimental study of cleaning device for wheat harvester based on CFD-DEM. *INMATEH Agricultural Engineering*, Vol. 75, Issue 1, pp. 571-583. DOI: https://doi.org/10.35633/inmateh-75-49.
- [18] Yu, C., Lin, D., Xu, N., Wang, X., Pu, K., Wang, Z., Zhao, G., Geng, R., & Gong, S. (2023). DEM simulation of particle flow and separation in a vibrating flip-flow screen. *Particuology*, Vol. 2023, Issue 2, pp. 113-127.
- [19] Zhang, Q., Zheng, Z., Liao, Q., Yu, L., Liao, Y., & Wan, X. (2025). Application status and prospect of coupled simulation in agricultural engineering research. *Transactions of the Chinese Society for Agricultural Machinery*, Vol. 56, Issue 7, pp. 20-37+145.
- [20] Zhang, X., Du, D., Man, T., Ge, Z., & Huppert, H. E. (2024). Particle clogging mechanisms in hyporheic exchange with coupled lattice Boltzmann discrete element simulations. *Physics of Fluids*, Vol. 36, Issue 1 Pt. 2, pp. 13312-13325.